Quantum Science and
Technology

Entanglement-informed construction of variational quantum circuits

To cite this article: Alina Joch *et al* 2025 *Quantum Sci. Technol.* **10** 035032

IOP Publishing Quantum Sci. Technol. 10 (2025) 035032 https://doi.org/10.1088/2058-9565/addb6f

Quantum Science and Technology

OPEN ACCESS

RECEIVED
29 January 2025

REVISED
8 May 2025

ACCEPTED FOR PUBLICATION
21 May 2025

PUBLISHED
29 May 2025

PAPER

Entanglement-informed construction of variational quantum circuits

Alina Joch[1,2], **Götz S Uhrig**[1] **and Benedikt Fauseweh**[1,2,*]

[1] Condensed Matter Theory, TU Dortmund University, Otto-Hahn-Straße 4, 44227 Dortmund, Germany
[2] Institute of Software Technology, German Aerospace Center (DLR), 51147 Cologne, Germany
[*] Author to whom any correspondence should be addressed.

E-mail: benedikt.fauseweh@tu-dortmund.de, alina.joch@tu-dortmund.de and goetz.uhrig@tu-dortmund.de

Keywords: variational quantum algorithms, entanglement spectrum, renormalization group

Abstract

The variational quantum eigensolver is a promising tool for simulating ground states of quantum many-body systems on noisy quantum computers. Its effectiveness relies heavily on the ansatz, which must be both hardware-efficient for implementation on noisy hardware and problem-specific to avoid local minima and convergence problems. In this article, we explore entanglement-informed ansatz schemes that naturally emerge from specific models, aiming to balance accuracy with minimal use of two-qubit entangling gates. We investigate three models of quasi-1D Hamiltonians focusing on entanglement barriers and long-range interactions. We find that including the entanglement structure in the parameterized quantum circuit reduces the resources necessary to achieve a given accuracy. A better assessment is obtained by analyzing how the ansatz captures the entanglement spectrum. Our comprehensive analysis provides a new perspective on the design of ansätze based on the expected entanglement structure of the approximated state.

1. Introduction

Since Feynman proposed using quantum computers to simulate quantum mechanical systems [1], various technologies have emerged as platforms for quantum simulation, for an overview see [2]. However, the development of large-scale, fault-tolerant quantum computers remains a significant challenge. Currently, only noisy intermediate-scale quantum (NISQ) devices [3] are available. Noise is a central problem, originating from various sources, such as system-environment interactions, inaccurate gate operations and unwanted interactions between qubits. It leads to errors in the calculations with NISQ devices, which can significantly affect the reliability and accuracy of calculations and complicates the simulation of complex quantum mechanical systems. Error correction methods required for large, fault-tolerant quantum computers are not yet fully realized. Therefore, a reduction of quantum circuits to a minimal number of gates and qubits is necessary [4–7].

In order to still take advantage of these devices, special algorithms have been developed to fulfill these restrictions [8]. One promising approach is the use of hybrid classical-quantum algorithms, such as variational quantum algorithms (VQAs) [8–13]. VQAs address computational tasks through a combination of classical and quantum computation. In these algorithms, the quantum computation involves a parameterized quantum circuit, the ansatz, that depends on a set of classical parameters, such as the rotation angles of single-qubit gates. These parameters are optimized iteratively through classical computation by minimizing a cost function designed such that its minima correspond to the solution of the computational problem. Through several quantum–classical optimization loops, the optimal parameters are identified.

One of the most prominent VQAs is the variational quantum eigensolver (VQE) [9, 14], which is used to provide an approximation to the ground state of many-body quantum systems through a unitary transformation of the computational basis state. The circuit ansatz typically consists of several layers of the same set of quantum gates. In principle, the accuracy of the optimized VQE results increases with the number of layers used [15].

On NISQ devices increasing the number of layers also introduces higher levels of noise due to the increased depth of the quantum circuit. Additionally, deeper VQE circuits exhibit the barren plateau phenomenon, making it exponentially harder to optimize the circuit due to a vanishing gradient [16], even on fault-tolerant quantum computers. Therefore, choosing an appropriate ansatz is a key task to enhance the accuracy, noise robustness, and optimizability of VQE [17, 18]. In the current literature, numerous approaches to design the ansatz for VQE are discussed and evaluated [19]. These approaches vary in structure and complexity, and present different challenges. Hardware-efficient ansätze are optimized for the architecture of the given quantum computer and normally have a low circuit depth making them faster and more robust against noise. However, their expressiveness can be limited, which can lead to suboptimal results for strongly correlated states. In contrast, problem-based approaches are specifically tailored to the problem to be solved and use more complex, deeper circuits that are able to better capture the specific properties of complex quantum many-body systems. These approaches offer higher expressive power and can provide more accurate results, but are more susceptible to noise and require longer execution times.

A critical aspect of all of these approaches is the role of entanglement, which serves as a valuable resource necessary for achieving the desired accuracy with a given circuit depth. Therefore, it is crucial to understand how a circuit captures the entanglement structure of complex ground states. Additionally, it is of fundamental interest to understand how different ansatz circuits converge and how the underlying entanglement of the approximated state affects this convergence [15, 20–22].

In this paper, we investigate three distinct models in which an ansatz emerges naturally due to the structure and interaction strength of the terms in the Hamiltonian. In the first case, we investigate systems with an impurity that acts as entanglement barrier. Here, we aim to reduce the number of gates that entangle the different subsystems separated by the impurity.

The second and third case focuses on quantum critical systems and systems with long-range entanglement, as they are especially challenging for VQE [23]. We will investigate whether singlets on long-range interacting dimers as an initial state can decrease the number of layers while still achieving a desired accuracy in both cases. Besides the accuracy in the energy, we also investigate the two approaches through the lens of entanglement spectra. Understanding entanglement properties of strongly correlated systems with and without disorder is of significant interest in the condensed matter community [24–26]. Additionally, it is also started to be used to understand the behavior of quantum circuits in VQA [15, 27, 28].

The article is set up as follows. Section 2 explains the methods used including a more detailed description of the VQE and information about the simulation. In section 3, we start with the impurity model explaining the model itself, the chosen ansatz and the results for energy and entanglement. Subsequently, in section 4 we investigate systems with competing long-range and short-range interactions transitioning from a long-range singlet to a quantum critical state. Then, in section 5 we discuss a random quantum critical system. Finally, we conclude in section 6.

2. Methods

2.1. VQE

The quantum circuit of the VQE depending on a set of parameters represents a unitary $U(\vec{\theta})$. The goal of the VQE is to find a set of parameters $\vec{\theta}$, such that $U(\vec{\theta})$ acting on the product state $|0\rangle^{\otimes n}$ approximates the ground state of a given Hamiltonian H of a system with n qubits.

For this, we use quantum–classical optimization loops: by applying the circuit with any choice of parameters $\vec{\theta}$ to the initial state we obtain a trial wave function $|\psi(\vec{\theta})\rangle = U(\vec{\theta})|0\rangle^{\otimes n}$. With this trial wave function, we can calculate the cost function in a next step. The cost function to find the ground state of the system is given by the expectation value of the energy depending on the given wave function $E_{\vec{\theta}} = \langle\psi(\vec{\theta})|H|\psi(\vec{\theta})\rangle$. The cost function is minimized with a classical optimization algorithm to find the best parameters $\vec{\theta}_{\mathrm{opt}} = \mathrm{argmin}_{\vec{\theta}} E_{\vec{\theta}}$. With the optimized parameters we then find the best approximation of the ground state of the Hamiltonian $|\psi(\vec{\theta}_{\mathrm{opt}})\rangle = U(\vec{\theta}_{\mathrm{opt}})|0\rangle^{\otimes n}$ obtainable with the given quantum circuit.

Quantum states prepared by parameterized quantum circuits offer enhanced expressivity in terms of captured entanglement compared to low-rank tensor states that can be computed classically [29, 30]. The VQE can therefore be effectively compared to classical variational methods such as tensor networks [31] and variational Monte Carlo [32].

2.2. Simulation

We use the Julia package Yao for quantum circuit simulations [33] and the Broyden–Fletcher–Goldfarb–Shanno method implemented in Optim.jl [34] for the classical optimization step. When calling the function *optimize* of Optim.jl we set the tolerances in changes of the function value and the gradient to 10^{-38} and the maximum number of iterations to 10 000. As initial values for the parameters $\vec{\theta}$ for $m+1$ layers, we use the result of m layers and add random numbers close to zero for the additional parameters for the added layer. This reduces the total number of required iterations and increases the precision of the results [17], which is one of the main difficulties here, especially for large numbers of layers. The long-range interaction models require several runs with different random numbers to ensure that the results converge.

For comparison, we compute the exact energy E and exact ground state $|\psi\rangle$ using the eigsolve function from KrylovKit.jl [35], which finds the smallest eigenvalues and their corresponding eigenvectors of a matrix using the Lanzcos algorithm.

For system sizes of up to 12 qubits, the calculations are performed with double precision making it in principle possible to achieve relative accuracies of up to 10^{-16}. As the number of qubits and layers increases, the simulation time increases rapidly. Therefore, for more than 12 qubits, we simulate the quantum circuit calculations on graphical processors using single precision, which reduces the possible accuracy of the overall calculation to roughly 10^{-8}.

3. Local impurity model

The first model we investigate is the analytically solvable transverse field Ising model (TFIM) [36, 37] with a central impurity qubit. Its Hamiltonian is given by

$$H_{\mathrm{TFIM}} = \sum_{i=-L/2}^{L/2} \left(-\sigma_i^z \sigma_{i+1}^z + h^x \sigma_i^x\right) + h_0^z \sigma_0^z, \tag{1}$$

where h^x is the disordering magnetic field. The last term describes a longitudinal field at the central qubit of the chain. Without longitudinal field and for $|h^x| < 1$, the system is in a ferromagnetic phase with all qubits being aligned along the z direction for $|h^x| \to 0$. For $|h^x| > 1$, the system is in a paramagnetic phase. In the limit of $|h^x| \to \infty$, all qubits are aligned along the x direction. Between the two phases, at $|h^x| = 1$, there is a quantum critical point, where the system is gapless. In our studies, we will focus on the critical point with $h^x = -1$. The model is visualized in figure 1.

We calculate the ground state energy numerically by diagonalization making it possible to compare these results with the results obtained with VQE. We will in all cases use open boundary conditions.

3.1. Circuit for local impurity model

Naturally, the achievable accuracy of the VQE depends on the chosen layout of the quantum circuit.

For the local impurity model, we will use a quantum circuit built from single-qubit rotations containing R_x and R_z gates on all qubits followed by two-qubit R_{zz} gates applied in a linear chain as shown in figure 2. This forms one layer of the quantum circuit which can be applied several times. We choose the R_{zz} gate instead of the often used CNOT gate, so that a single layer can always be initialized as the identity and $m+1$ layers have at least the same accuracy as m layers.

The accuracy of the VQE approach for a fixed circuit geometry was studied for these models without impurities in [15]. Here, we want to focus on the influence of different numbers and positions of entangling gates on the accuracy of the optimized circuits.

The most interesting choice is to investigate gates on the central qubit, i.e. we will vary the number of layers in which gates are applied to the impurity qubit. As notation we will use $x =$ ('layers including gates applied to the central qubit'). The ansatz of the circuit together with this notation is visualized in figure 2.

Such an approach makes a technique called circuit cutting [38–40] attractive: the quantum circuit is cut at several points and the smaller sub-circuits are evaluated separately on a quantum computer. The information of the different parts is exchanged classically. Since the classical information exchange is costly, it is only reasonable to use this method, if few cuts are sufficient in order to be able to reach accurate results. However, in systems where this is possible, circuit cutting significantly reduces the number of quantum gates as well as qubits in a calculation, which can further streamline VQE approaches by decreasing the hardware demands and potentially mitigating errors introduced through gate operations. Therefore, one goal is to reduce the number of layers including gates applied to the central spin, i.e. the numbers in x, while still achieving high accuracy.

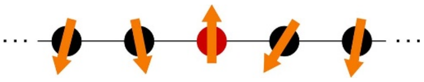

Figure 1. The impurity model is depicted. The qubit in the center marked in red is subject to a strong longitudinal magnetic field.

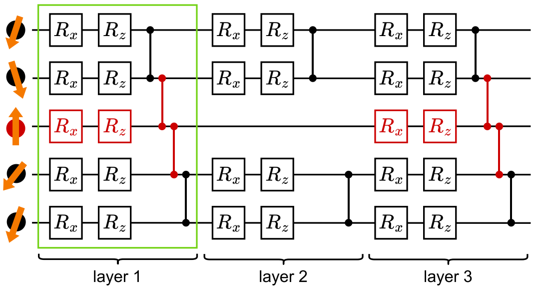

Figure 2. Variational quantum ansatz used in the simulations of the impurity model depicted exemplarily for five qubits and three layers. One layer is indicated by the green box consisting of a R_x and a R_z rotation applied to each qubit followed by R_{zz} gates. The gates marked in red are only included in the layer if its number is included in x, i.e. here $x=[1,3]$.

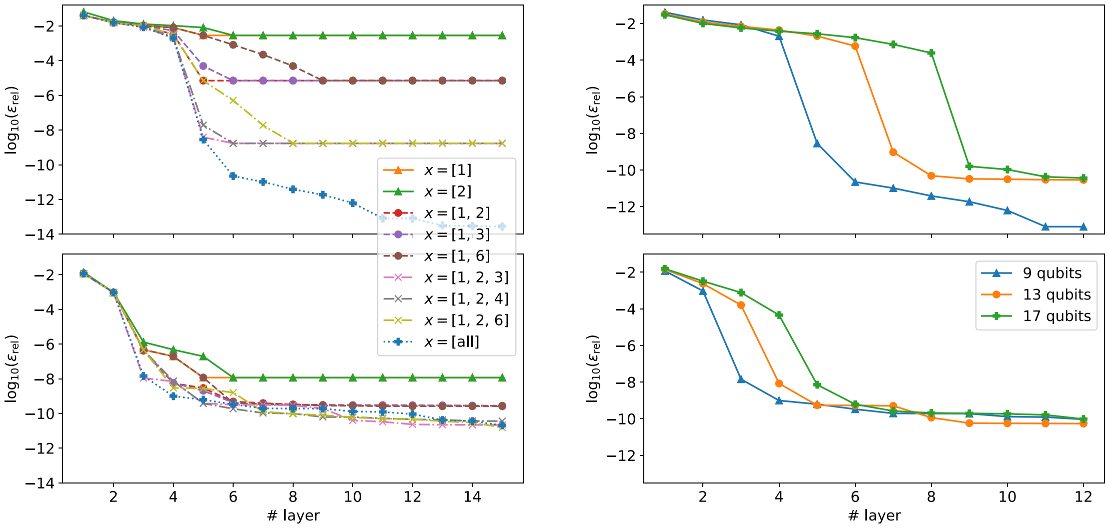

(a) (b)

Figure 3. (a) Accuracy obtained by the VQE for the TFIM at $h^x=-1$ without impurity, $h_0^z=0$, (top) and with impurity, $h_0^z=-10$, (bottom) for 9 qubits compared to the exact result in a logarithmic plot. Results for various positions of entangling gates x are shown. (b) Accuracy depending on the number of layers for the TFIM with $x=[\mathrm{all}]$ for varying system size without impurity, $h_0^z=0$, (top) and with impurity, $h_0^z=-10$, (bottom).

3.2. Results for local impurity model

3.2.1. Energy

In the following, the optimized energy $E'=E_{\vec{\theta}_{\mathrm{opt}}}$ is calculated depending on, (i) total number of layers, (ii) number of lattice sites, (iii) field strength h_0^z and (iv) layers in x. The results are compared with the exact result E by computing the relative error $\varepsilon_{\mathrm{rel}}=|E-E'|/|E|$.

An overview of the results for 9 qubits in the TFIM model is shown in figure 3(a). Accuracy plateaus which form after a sufficient number of layers are our primary finding. The value of the plateau only depends on the absolute number of entangling layers: by adding a layer to x the value of the plateau is decreased, i.e. the accuracy of the ansatz improves. However, the earlier the entanglement gates are applied in the algorithm, the sooner the plateau value is reached.

Comparing the impurity problem and the problem without impurity in figure 3(a), one can see that the value of the plateau improves drastically when including an impurity even for the VQE with only a single entangling layer. Here, we find an increase of the groundstate energy accuracy of several orders of magnitude.

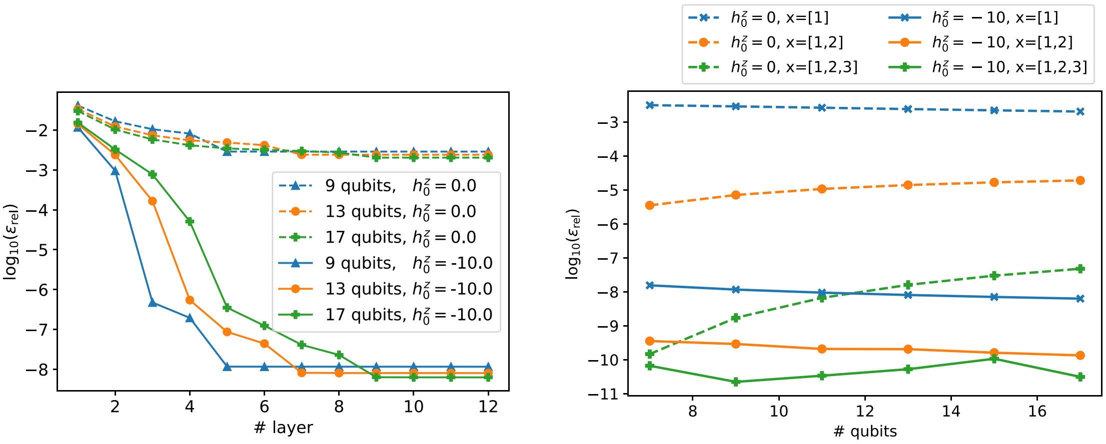

(a) (b)

Figure 4. (a) Accuracy depending on the number of layers for the TFIM with $x = [1]$ for varying system size without impurity, $h_0^z = 0$, and with impurity, $h_0^z = -10$. (b) Logarithmic accuracy obtained by the VQE compared to the exact result for different system sizes as well as number of layers in x for the TFIM at the critical point.

In critical phases, two regimes have been observed for the convergence behavior [15]: for small numbers of layers the accuracy improves slowly independent of the system size. This regime is called finite-depth regime. After a critical number of layers, a finite-size regime starts. In this regime, the accuracy improves again exponentially. This behavior can also be seen in our results in figure 3(a) for 9 qubits. Comparing the results with and without impurity, a major difference is recognized with respect to the transition to an exponential convergence in accuracy: with impurity the number of layers needed to reach exponential improvement is halved. To investigate this further, we computed the accuracy depending on the number of layers for $x = [\text{all}]$, where 'all' means that every layer is included in x, for various system sizes, visualized in figure 3(b).

Without impurity, we can reproduce the results from [15]: First, we see a finite-depth regime followed by a finite-size regime depending linearly on the system size, where an exponential improvement in accuracy is achieved (the plateaus at high numbers of layers are formed due to finite precision). The separation into these two regimes is an important difference compared to gapped phases. With impurity, we can see in figure 3(b) also for other system sizes that the finite-depth regime is halved. This behavior can be explained by the bisection of the chain induced by the impurity. The variational algorithm needs only half of the layers as without impurity to realize that the system is finite.

In figure 4(a), we investigate the case $x = [1]$ for various system sizes. Without impurity, we can reach only a limited accuracy due to the high plateau value. In contrast, the plateau with impurity is much lower and is almost independent of system size. Interestingly, by including the impurity, the finite-size regime, i.e. the exponential behavior, is halved, but the plateau requires the same number of layers to be reached as without impurity.

To scale this approach, it is important to investigate the plateau values for different x for increasing system sizes to reach a better insight into how much the plateau values improve with impurity. In figure 4(b), this is shown for $x = [1], x = [1,2]$ and $x = [1,2,3]$. We can see that by increasing the number of layers in x the accuracy of the result increases for all chain lengths. Without impurity, the plateau values are much higher than with impurity. All results seem to slowly converge to finite values. This indicates that both, impurity strength h_0^z and number of layers between subsystems x remain relevant on all length scales.

The number of entries in x is the number of layers where gates are applied to the central spin. Therefore, it indicates the number of cuts that would be necessary to divide the circuit as one cut is needed for every full layer. Thus, from figure 4(b) one can read off the number of cuts necessary to achieve a given accuracy.

3.2.2. Entanglement entropy and spectrum

To further understand the previous results in terms of entanglement properties, we first investigate the entanglement entropy. We, therefore, compute the reduced density matrix of the exact ground state $|\psi\rangle$

$$\rho_{\rm A} = \text{Tr}_{\rm B} |\psi\rangle\langle\psi| \tag{2}$$

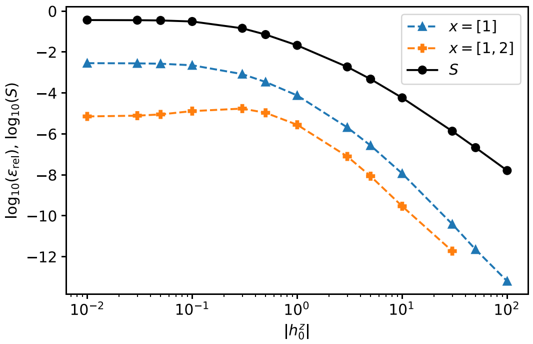

Figure 5. Logarithmic accuracy obtained with the VQE at the plateau for $x = [1]$ and $x = [1,2]$ compared to the entanglement entropy for varying impurity strength for the TFIM with 9 qubits.

with A being the left half of the chain and B the right half including the central qubit. The entanglement entropy is given by

$$S = -\mathrm{Tr}\left(\rho_{\rm A}\ln\left(\rho_{\rm A}\right)\right) . \tag{3}$$

To better understand the improvement in accuracy when adding an impurity, we plot the exact entanglement entropy as function of h_0^z and the relative energy error $\varepsilon_{\rm rel}$ for $x = [1]$ and $x = [1,2]$ in figure 5.

For increasing magnetic field strength, the entanglement entropy decreases and at the same time the accuracy improves, following the same trend. Interestingly, increasing the number of layers in x seems to have an almost constant effect on the relative accuracy improvement for weak as well as for strong impurity field strength h_0^z.

In a second step, we investigate the entanglement spectrum to better understand the improvement in accuracy with increasing number of layers in x. The entanglement spectrum is given by the eigenvalues of the entanglement Hamiltonian

$$H_{\rm ent} = -\ln\left(\rho_{\rm A}\right) . \tag{4}$$

We compare the entanglement spectrum of the exact ground state $|\psi\rangle$ with the entanglement spectrum of the variational state $|\psi(\vec{\theta})\rangle$.

In figure 6(a), we first study the entanglement spectrum for the TFIM with 9 qubits without impurity for $x = [\text{all}]$ depending on the total number of layers. It can be seen that for small numbers of layers only the first eigenvalue, $k = 1$, is captured well and up to four layers the accuracy improves slowly. With five layers, however, all eigenvalues up to a value of around 25 are calculated correctly by the VQE calculation. This fits the transition of the regimes, as for 9 qubits without impurity the exponential behavior is reached after the fourth layer, see figure 3(b). Larger eigenvalues are not reproduced correctly even with five layers due to the given precision in the calculation, as high eigenvalues of the energy entanglement spectrum correspond to extremely small values in the reduced density matrix. Hence, only very precise numerics is able to evaluate them reliably.

In figure 6(b), the entanglement spectrum is shown for the TFIM with 9 qubits with and without impurity for 13 layers for different x. By increasing the number of layers included in x, we iteratively capture more eigenvalues with the VQE approach starting with the small, most significant eigenvalues. In particular, in the case without impurity the number of correctly found eigenvalues is doubled with each additional layer in x. The largest eigenvalues are not calculated correctly even in the case of $x = [\text{all}]$. This is again due to the precision of the calculation.

When comparing the exact eigenvalues of the systems with and without impurity, it becomes clear that the TFIM without impurity has many more eigenvalues with a significant contribution to the spectrum. Therefore, any VQE algorithm has to reproduce these eigenvalues correctly for an accurate description of the groundstate, while in the case with impurity only the first few values are necessary. Therefore, even for the strongly simplified circuits with only one or two entangling layers, the algorithm can be expected to yield accurate groundstate energies although the approach captures only the first few eigenvalues of the entanglement spectrum. The other eigenvalues are much larger, hence much less significant.

In addition to the aforementioned results, we also investigated the behavior of energy accuracy and of entanglement entropy and spectrum for the XXZ chain. The findings are comparable to those observed for the TFIM, with only minor deviations. The results are presented in appendix B.

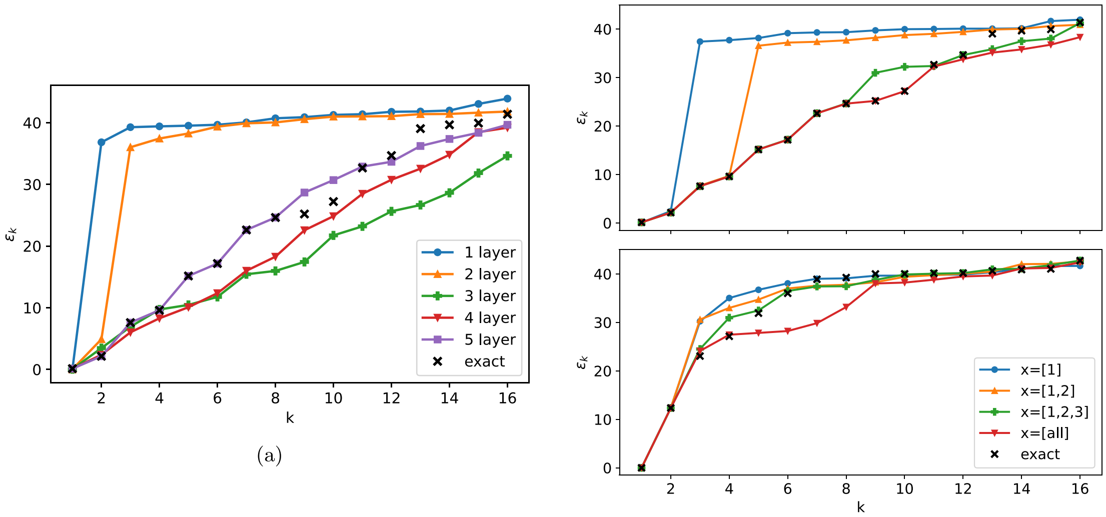

(a)

(b)

Figure 6. (a) Eigenvalues ε_k of the entanglement Hamiltonian for the TFIM at the critical point with 9 qubits without impurity for $x = [\text{all}]$ depending on the number of layers compared to the exact solution. The index k indicates the kth eigenvalue. (b) Eigenvalues ε_k of the entanglement Hamiltonian for the TFIM at $h^x = -1$ with 9 qubits without, $h_0^z = 0$, (top) and with impurity, $h_0^z = -10$, (bottom) impurity for 13 layer for different x compared to the exact solution.

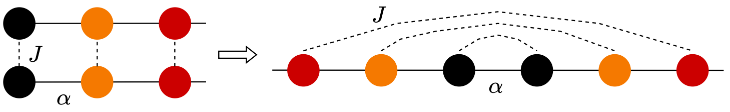

Figure 7. The long-range entanglement model is depicted. It is given by a qubit ladder mapped to an one dimensional system. Direct neighbors are coupled with the coupling constant α, the long-range interactions by J.

3.2.3. Magnitude of gradient

So far, we showed that in impurity models we can significantly reduce the number of entangling gates at this impurity while maintaining high accuracy. This is advantageous for the use of circuit cutting techniques and for reducing potentially mitigating errors introduced by gate operations. An additional benefit of this approach is that it addresses the problem of barren plateaus. By reducing the expressivity of our ansatz through a reduction of entangling gates, the distance of the circuit to a 2-design is increased, which has recently been connected to the magnitude of the gradient in circuit optimization [41]. This is shown in further calculations in appendix A. As the variance of the gradient is approaching zero much faster when using the full ansatz, barren plateaus and optimization problems appear already with less layers and less qubits compared to the reduced ansatz. Therefore, especially for large systems the reduced ansatz will be a noticeably better choice in terms of optimization. We conclude that our reduced ansatz scheme is to be preferred over the full conventional ansatz, i.e. an ansatz with no reduction in entangling gates, in terms of circuit cutting techniques, reduced errors and improved optimization capability.

4. Long-range entanglement model

We want to investigate the influence of non-product initial states and of short- and long-range ansatz schemes on the accuracy of VQE. For this aim, we study the Heisenberg chain with additional long-range couplings, described by the Hamiltonian

$$H_{\text{SL}} = \alpha \sum_{i=1}^{n} \left(\vec{S}_i \cdot \vec{S}_{i+1} \right) + J \sum_{i=1}^{n/2} \left(\vec{S}_i \cdot \vec{S}_{n-(i-1)} \right), \tag{5}$$

with n being an even total number of qubits in the chain. Note that equation (5) can be described by a qubit ladder mapped to a one dimensional chain. For different values of α and J, we obtain a critical to dislocal entanglement crossover, i.e. the entanglement entropy of a central bipartition of the system behaves as $S(\rho_I) \propto C\log(n)$ for the case $\alpha \gg J$ while $S(\rho_I) \propto n$ for $J \gg \alpha$. The model is visualized in figure 7.

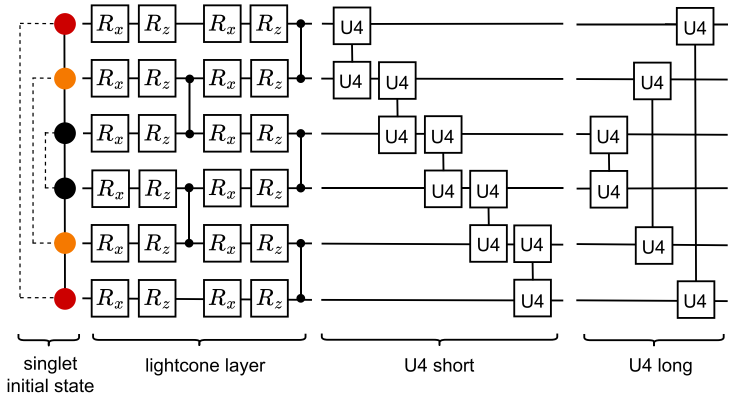

Figure 8. Variational quantum ansätze used in the simulations of the long-range entanglement model exemplarily depicted for 6 qubits. From left to right: singlet initial state is constructed by building singlets between qubits with the same color, the dashed line indicates J couplings and the solid line α couplings of equation (5); one single lightcone layer consisting of the single qubit rotation gates R_x and R_z and the entangling gates R_{zz}; set of $U4$ gates entangling neighboring qubits; $U4$ gates entangling qubit pairs which form singlets in the singlet initial state.

Similar models, often called rainbow chains, were also studied in other works showing interesting scaling behavior of the entanglement entropy [42, 43].

4.1. Circuit for long-range entanglement model

We investigate the influence of changing the initial state to which the variational ansatz is applied, and the influence of including the long-range entanglement structure of the system into the variational circuit. The chosen circuits and gate sets are depicted in figure 8. For the initial state, singlets are built between qubits which match the long-range interactions induced by the second part of equation (5). This is visualized in figure 8 by dots that have the same color. We combine this singlet initial state with a varying number of lightcone layers (also visualized in figure 8) and compare it with a lightcone layer applied to a product initial state. The two-qubit gates in the lightcone layer are R_{zz} gates. Such lightcone layers are typically used in dense hardware efficient ansatz schemes. Additionally, we investigate the effect of matching the short- and long-range interactions in the variational circuit using a general $U4$ two-qubit gate. The $U4$ gate is implemented optimally as described in figure 7 of [44].

4.2. Results for the long-range entanglement model

4.2.1. Energy

We start to investigate the model in equation (5) for large ratios $J/\alpha \gg 1$. As for the impurity model, we start by focusing on the relative energy error. The results are presented in figure 9(a) for 6 qubits where we compare an initial product state with an initial singlet state. Different numbers of lightcone layers are added to the initial states. We choose to switch to the lightcone layer because the convergence was improved sligthly compared to the ansatz structure used for the impurity model.

We can observe that increasing the value of J/α leads to an improvement in the results with singlet initial states. This difference is directly present without a variational layer. Additionally, the findings for 8 and for 10 qubits are plotted for one layer with singlet initial state. We can see that there is no dependence on the system size, as the accuracy is maintained for different qubit chain lengths when comparing the same value of α. This is consistent with the results of [28], which demonstrated for correlated topological phases that with an initial state fitting the given structure of the system one variational layer is sufficient to achieve good results independent of the system size. If the desired accuracy is in the range of 10^{-2} to 10^{-6}, the solution with singlet initial state and one variational layer is already good enough. In contrast, starting from a product state, multiple variational layers are necessary to achieve the same level of accuracy.

However, the accuracy depends directly on the ratio J/α. For $\alpha \approx J$, the accuracy decreases towards the value obtained with product initial state. At the same time, the number of layers needed to converge to higher accuracy does not differ significantly between the two initial states, i.e. in figure 9(a) 4 to 5 layers are necessary in both cases. For larger system sizes, even more layers are needed. It follows that either if (i) $\alpha \approx J$ or if (ii) $\alpha < J$ and higher accuracies are desired, the singlet initial state does no longer yield an improvement to the product initial state. It is therefore of interest to identify an ansatz that can be used to achieve higher accuracy with a single layer. Moreover, with the ansatz chosen so far consisting of R_{zz}-entangling gates, we find bad convergence behavior during optimization. Using $U4$ instead of R_{zz} gates showed to improve the

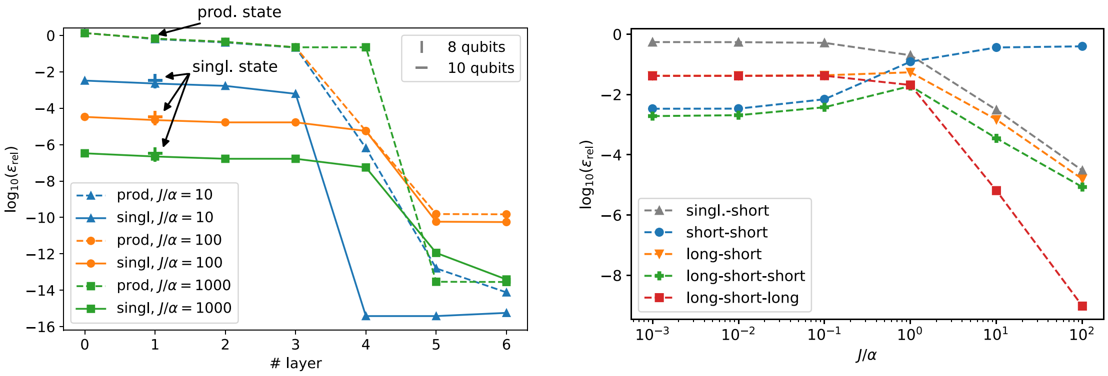

(a) (b)

Figure 9. (a) Accuracy of energy obtained with VQE for 6 qubits for various ratios J/α. Additionally, for one layer the results for 8 and 10 qubits are depicted. (b) Comparison of accuracies obtained with different combinations of *U*4 short and *U*4 long gate sets (see figure 8) forming one layer for varying ratio of α and *J* for 10 qubits. Additionally, the results with initial singlet state and one *U*4 short gate set (singl.-short) are shown in grey for comparison.

convergence. Consequently, we employ a *U*4-layer ansatz to find the best solution with only one layer. Note that the *U*4 gate has many more free parameters leading to an improved accuracy but also a longer runtime.

A first approach is to replace the initial singlet state by a dimerized variational layer. We study if having optimizable parameters between the long-range coupled qubits improves the results further. We use *U*4-gates between the qubits coupled by *J*. This then builds one *U*4 long gate set as described in section 4.1. In figure 9(b), the accuracies obtained with different combinations of the *U*4 long gate set with a *U*4 short gate set are compared for different ratios of α and *J*. For comparison, also the results with initial singlet state and one short gate set are shown in grey.

For the singlet initial state combined with an *U*4 short gate set (singl.-short), we observe that for $J \gg \alpha$ this choice leads to results already in the order of 10^{-4} analogously to the results obtained before with a lightcone layer applied to the singlet initial state. For smaller *J*, the accuracy decreases. Comparing this with the ansätze with product initial state, we see that using the *U*4 long gate set, especially more than once, yields an improvement to the singlet initial state for all ratios J/α. In general, we find three regimes: for $J \ll \alpha$, the *U*4 short gate set gives the best results and an additional *U*4 long gate set only has a small impact. For $J \approx \alpha$, we have an intermediate regime and for $J \gg \alpha$, the ansatz with two *U*4 long gate sets gives a large improvement compared to other ansätze. For $J/\alpha = 100$, we even reach accuracies in the order of 10^{-8} with only a single layer. In a next step, we check if this result is also valid for larger system sizes.

In figure 10(a), we show the dependence of the different ansätze on the system size for $J/\alpha = 100$. The accuracy obtained with the long-short-short ansatz decreases for larger system sizes. This indicates that for small systems the short gate set is still sufficient to capture the long-range interactions which is no longer the case for larger system sizes. However, the other ansätze converge to a constant accuracy for larger system sizes. As for the solution with singlet initial state and one variational layer shown in figure 9(a), we find a system size independent behavior.

It follows that we can already identify the long-short-long ansatz as a good choice for $J \gg \alpha$. However, we can see in figure 9(b) that for $J \to \alpha$ the accuracy is worse than 10^{-4} even with the long-short-long ansatz. Therefore, we investigate in a next step whether applying a small number of layers of an ansatz including *U*4 long gate sets provides an improvement compared to using only a single layer, which was not the case for the solutions obtained with an ansatz consisting only of gates between neighboring qubits as visible in figure 9(a). We compare the solution of an *U*4 short ansatz with the solution of an long-short ansatz for up to 4 layers. The results are depicted in figure 10(b) for $J/\alpha = 3$.

Comparing the results with the short ansatz, we find the typical behavior of a critical system with a finite-depth and a finite-size regime. That implies that the larger the system size is, the more layers are required to achieve an improvement in accuracy. For the long-short layer, we observe an exponential improvement in the finite-depth regime in contrast to the nearly constant behavior in the case of the short ansatz. Consequently, much better results can be obtained with only a few layers, which constitutes a great advantage especially for large system sizes. The number of layers necessary to obtain a certain accuracy depends on the ratio J/α: the larger the ratio, the fewer layers are required.

In conclusion, the singlet initial state provides an initial improvement to the accuracy. However, a combination of variational long-range and short-range gates facilitates convergence for the whole phase

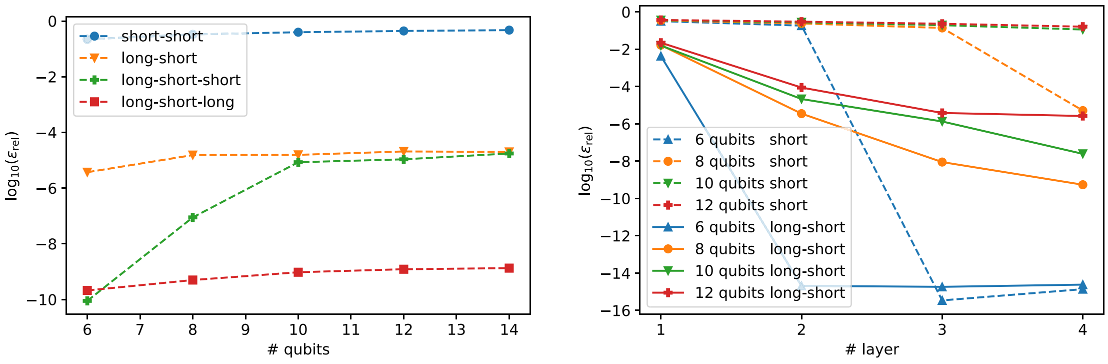

(a) (b)

Figure 10. (a) System size dependence of the different ansätze consisting of different combinations of *U*4 short and *U*4 long gate sets (see figure 8) for $J/\alpha = 100$. (b) Accuracy depending on the number of layers for a *U*4 short ansatz and a *U*4 long-short ansatz (see figure 8) for $J/\alpha = 3$ for various system sizes.

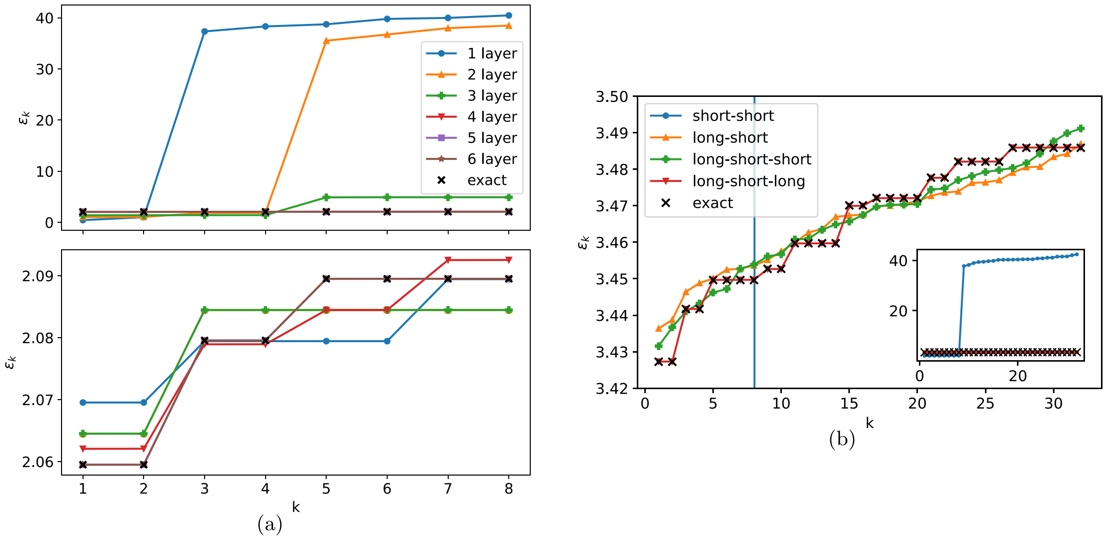

(a) (b)

Figure 11. (a) Entanglement spectrum for $J/\alpha = 100$ and 6 qubits. The upper plot shows the results with product initial state, the lower plot the results with singlet initial state. Note the different intervals of the ϵ_k-axis. (b) Entanglement spectrum for the different ansätze for 10 qubits and $J = 100$. The inset shows the behavior of the short-short ansatz.

space. Therefore, for achieving good accuracies with few parameters/layers, including the long-range structure into the variational circuit is the best choice.

4.2.2. Entanglement spectrum

As before, we also investigate the entanglement spectrum to obtain a better understanding of the different convergence behaviors. First, the entanglement spectrum for $J/\alpha = 100$ of the data shown in figure 9(a) is plotted for 6 qubits in figure 11(a).

First of all, when comparing the exact spectrum with the one shown in figure 6(b) we observe that the range of the values is small compared to the ones from the impurity model. This can be attributed to the high entanglement inherent in the qubit ladder model. In general, a global convergence is observed instead of finding the lowest eigenvalues first, which is due to the long-range entanglement. With singlet initial state the eigenvalues found with VQE are close to the exact ones already with one layer. In contrast, with product initial state the eigenvalues are close to the exact ones from the fourth layer onwards. This fits to the results of the accuracy in figure 9(a).

Next, in figure 11(b) we compare the accuracy of the calculated entanglement spectra of the different ansätze in figure 9(b) for $J/\alpha = 100$. The results obtained with the short-short ansatz are not even close to the exact ones, which changes as soon as one *U*4 long gate set is included in the ansatz. For the long-short-long ansatz, all eigenvalues are found correctly, while the number of parameters for this approach

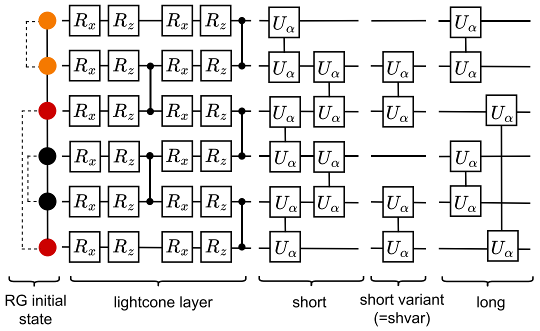

Figure 12. Variational quantum ansätze used in the simulations of the random quantum critical point model exemplarily depicted for 6 qubits and one possible outcome of the RG flow. From left to right: singlet initial state is constructed by building singlets between qubits with the same color, the dashed line indicates the singlets formed and the solid line the J couplings; one single lightcone layer consisting of the single qubit rotation gates R_x and R_z and the entangling gates R_{zz}; set of $U_\alpha := R_{xx}R_{yy}R_{zz}$ gates entangling qubits with the same structure as in the lightcone layer; U_α gates entangling qubit pairs with strongest couplings except for the ones coupled according to the RG flow—the number of gates is equal to half of the number of RG singlet pairs minus one; U_α gates entangling qubit pairs which form singlets according to the RG flow.

is approximately the same as for the short-short approach. It can thus be inferred that the long-short-long approach is the most suitable and outperforms a more conventional ansatz, e.g. the short-short ansatz.

5. Random quantum critical point model

The long-range entanglement model is inspired by random quantum critical qubit chains where entangled singlets are formed across the whole lattice in an emergent manner [45–47]. We investigate the random Heisenberg chain defined by

$$H_{\mathrm{RH}} = \sum_{i=1}^{n} J_i \vec{S}_i \cdot \vec{S}_{i+1} \,. \tag{6}$$

The couplings $J_i > 0$ are drawn from any non-singular distribution. The randomness in the couplings drives the system to a random critical point at long distances [47]. Non-local singlets occur in these systems according to the renormalization-group (RG) flow: iteratively, the strongest bond of the system is found and a singlet between the two qubits coupled by this bond is built. The neighboring qubits of the singlet are then coupled by a smaller renormalized coupling strength based on second-order perturbation theory. Iterating these two steps yields a very good approximation to the ground state of the system with singlets connecting arbitrarily distant sites, which is asymptotically correct for large disorder and large distances.

5.1. Circuit for the random quantum critical point model

For the random quantum critical point model, a similar approach to the one of the long-range entanglement model is used. The singlets of the singlet initial state are formed according to the long-range interactions resulting from the RG flow. This is exemplarily shown for one configuration in figure 12. We also apply lightcone layers to the different initial states and compare the accuracy of the results. To investigate the effect of using the RG singlet structure in the variational part of the circuit, we use $U_\alpha := R_{xx}R_{yy}R_{zz}$ gates, which stays within the $S = 1$ symmetry sector [48]. In the long gate set, the gate is applied to the qubits that form singlets according to the RG flow. The short gate set is structured as in a lightcone layer. A variant of this is to only apply gates to neighboring qubit pairs with the strongest couplings excluding those already coupled within the long gate set. This is done up to a number of half of the RG singlet pairs minus one. In this way combining the short variant with the long gate set gives as many gates as in the short ansatz making a direct comparison possible.

5.2. Results for the random quantum critical point model

In the random quantum critical point model singlets are formed randomly depending on the couplings. We consider always several configurations for the random couplings and take the average value for all quantities of interest of the different runs. The random coupling values J_i are sampled from the distribution

$$P(J) = \frac{1}{\delta} J^{-1+\delta^{-1}} \tag{7}$$

as suggested in [49] with a disorder strength $\delta \geqslant 1$. The larger δ, the larger is the disorder of the system.

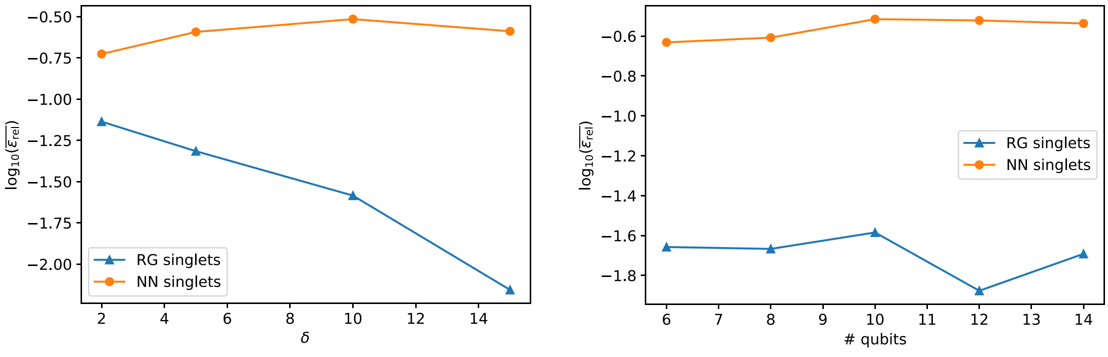

(a) (b)

Figure 13. (a) Energy accuracy for one lightcone layer for two initial states depending on the disorder strength δ for 10 qubits. It is averaged over 100 configurations of random coupling constants drawn from the distribution given in equation (7). (b) Energy accuracy depending on the system size for two initial states and one lightcone layer for $\delta = 10$ averaged over 100 configurations.

We start again by inspecting the result for a prepared initial state together with one lightcone layer for different values of δ. The chosen initial state consists of singlets between qubit pairs which form a singlet according to the RG flow: the two qubits coupled by the largest value J_i build a singlet. Under the condition $J_i \ll J_{i-1}, J_{i+1}$, the neighboring qubits are then coupled by a Heisenberg interaction with strength [47]

$$J'_{i-1,i+2} = \frac{J_{i-1}J_{i+1}}{2J_i} \tag{8}$$

resulting from second-order perturbation theory. These two steps are iterated until all qubits are paired to singlets. In this way, we get an initial state without any pre-training, but just by the classical RG flow calculation, which has a linear scaling with system size. When doing the simulation, we first determine the singlet pairs using the RG flow and then apply the variational circuit to a state consisting of those singlet pairs.

This is compared with singlets formed between neighboring qubits. The results are displayed in figure 13(a) for a system size of 10 qubits. The larger δ is, the better is the result for the RG initial state compared to the initial state with nearest neighbor (NN) singlets. This was to be expected, as large values of δ correspond to a distribution with rather disparate J values, in which case the RG approach works particularly well. Additionally, the result matches with the results from the last section, where we saw the same for increasing the ratio of J and α.

For a fixed value of δ, the results remain independent of system size, see figure 13(b).

When applying more layers to these initial states, starting from the second layer on, the results converge and the chosen initial state does no longer make any difference. Therefore, as for the long-range entanglement model, a next step to reach an overall improvement would be to include the entanglement structure of the system not only in the initial state, but in the circuit itself. However, the average length of the singlets grows only logarithmically with the system size as can be seen in figure 14(a).

To test whether incorporating the structure into the circuit itself works well, we investigate a system size of 120 qubits. To be able to simulate such a large system, we switched to tensor network calculations using quimb implemented in python [50]. In figure 14(b), we compare the accuracy of the results for (i) using NN singlets in the initial state combined with a short layer, for (ii) using RG singlets in the initial state combined with a short layer and for (iii) using RG singlets in the initial state combined with a layer consisting of short variant and a long gate set. The gate sets are depicted in figure 12. Note that all three ansätze used have the same number of gates and parameters. The accuracy is calculated for three values of δ.

The results show that the accuracy using an RG initial state increases with increasing δ in comparison to using singlets between neighboring qubits as the initial state. This outcome aligns with the result observed for 10 qubits in figure 13(a). Most importantly, if the structure resulting from the RG flow is adopted within the variational circuit itself, a subsequent enhancement is observed, exhibiting a similar magnitude to the previous one. It is evident that a well-chosen initial state and variational circuit significantly enhances the performance compared to purely local ansatz schemes, e.g. the NN short ansatz, given that the number of parameters remains constant across all three variants.

For investigating how this behavior scales with more layers, a system size of about 1000 qubits is an interesting choice. Since simulations with a classical computer are no longer feasible at this scale, it would be instructive to evaluate it on a real quantum device. We leave this question open for future investigations.

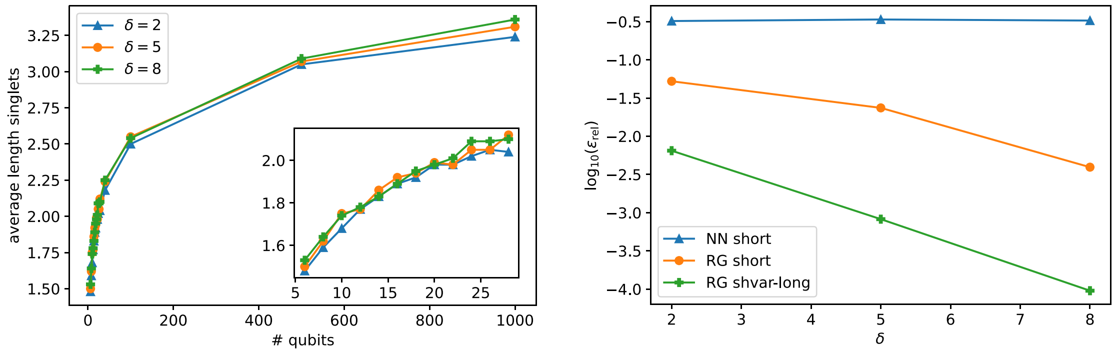

(a) (b)

Figure 14. (a) The average length of singlets given by the RG flow is plotted depending on the system size for different disorder strengths δ. Each length is calculated by averaging over 1000 configurations of random coupling constants. (b) Energy accuracy of the results for using NN singlets in the initial state combined with a short layer, for using RG singlets in the initial state combined with a U_α short layer and for using RG singlets in the initial state combined with a layer consisting of short variant (shvar) and a U_α long gate set depending on the disorder parameter δ. A system size of 120 qubits is used for the simulation to have an average length of singlets larger than two. The different gate sets are depicted in figure 12.

6. Conclusions

We provide an extensive study comparing entanglement adapted and conventional variational circuits for three classes of quasi-1D Hamiltonians. We focus on the convergence of the ground state energy and of the entanglement spectrum depending on the number of layers and the ansatz choice. For the impurity models, we found that plateaus are formed in the accuracy of the energy depending on the number of layers. The value of the plateau depends on the absolute number of entangling gates between the subsystems and the strength of the impurity. The entanglement spectrum shows an iterative convergence for the impurity models meaning that one eigenvalue after the other is captured by the VQE solution. For the long-range entanglement model, we show that including both the short-range and the long-range couplings in the variational circuit improves the convergence of the VQE. In contrast to the impurity model we observe global convergence of the almost flat entanglement spectrum. Using the insight from the long-range model, we demonstrate that renormalization group theory can be used to guide the design of efficient low-depth circuits for tackling the challenging class of random quantum critical points. By incorporating the hierarchical structure of the RG approach, our ansatz schemes significantly outperforms uninformed alternatives, which we showed for simulations on systems as large as 120 qubits.

Our results show that when the ansatz, i.e. the layout of the gates, follows the entanglement structure, higher accuracy or similar accuracy with lower cost of quantum resources (either number of qubits or gates) can be achieved, compared to conventional ansatz schemes. For the impurity models, we showed that our ansatz gives an improvement in terms of circuit cutting techniques, reduced errors and improved optimization capability. In case of long-range interactions our ansatz reduces the required circuit depth.

We conclude that the entanglement structure can inform the design of ansatz schemes, specifically for models with pronounced entanglement properties, like barriers in entanglement or long-range entanglement. A flat entanglement spectrum, typical for high level of entanglement, does not imply, that the system is hard to capture, if one adjusts the ansatz to the structure as in the case of the RG flow. For steep entanglement spectra, one only needs to use few entangling gates between subsystems without loss of accuracy. These results open a new path in understanding the convergence of variational quantum circuits based on the global properties of the entanglement spectrum.

The results are of high interest for various models. Examples for impurity models that would be interesting to be investigated with our results are the Anderson model used to describe electrons in (heterostructure) quantum dots [51], the Kondo model which has emerged as an important tool for understanding the behavior of strongly correlated systems and continues to offer considerable promise [52, 53], and for simulations of molecules [8]. Moreover, long-range interactions play a role in numerous physical phenomena, making them a crucial field of investigation [54, 55]. Future work may also be directed towards the application of the developed ansätze to the aforementioned systems on NISQ devices, as the models are of great physical interest. As our results specifically address the issues associated with NISQ devices, they offer the potential to gain interesting insight into the various models using current quantum computing platforms. Finally, the reduction of the barren plateau problem was observed. It remains an open question to determine whether this is a systemic feature of entanglement information-based ansatz schemes, which would suggest that such schemes have even greater efficacy.

Data availability statement

All data that support the findings of this study are included within the article (and any supplementary files).

Acknowledgments

This work has been supported by the Quantum Fellowship Program of the German Aerospace Center (DLR). We thank F Eickhoff and K Lively for helpful discussions.

Appendix A. Magnitude of the gradient in the impurity model

Here, we show that the reduced ansatz for the impurity model addresses the problem of barren plateaus. To this end, we examine the gradient for both the full ($x = [\text{all}]$) and the reduced ($x = [1]$) ansatz for different numbers of layers and qubits for the TFIM model with impurity.

While the mean of the gradient for random choices of $\vec{\theta}$ is zero, the variance can be larger. A larger variance is advantageous for the minimization as non-zero elements are needed to find a direction for the next minimization step. It was shown that the variance approaches zero for increased circuit depth and system size [16, 41]. We first investigate the distribution of the variance of the gradient over all parameter choices in figure 15(a) for one choice of circuit depth and system size. In the case of the reduced ansatz, there is one parameter which has a much larger variance than all other parameters. This is the first rotation angle applied to the impurity and this large value is also present for other system sizes and circuit depths. This means that the minimization algorithm can optimize in that direction. All other parameters have much smaller variances, all in the same order of magnitude. Therefore, we want to have a closer look at the behavior of those parameters to get an idea about the risk of barren plateaus for the case that the parameter with large variance is already optimized.

An examination of the variance of the gradient of the remaining parameters is shown in figure 15(b) with respect to system size. It reveals that the slope of the reduced ansatz is, on average, reduced in comparison to that of the full ansatz. This means that with the reduced ansatz the problem of barren plateaus is decreased even without the parameter with large variance as there are statistically more non-zero values for minimization.

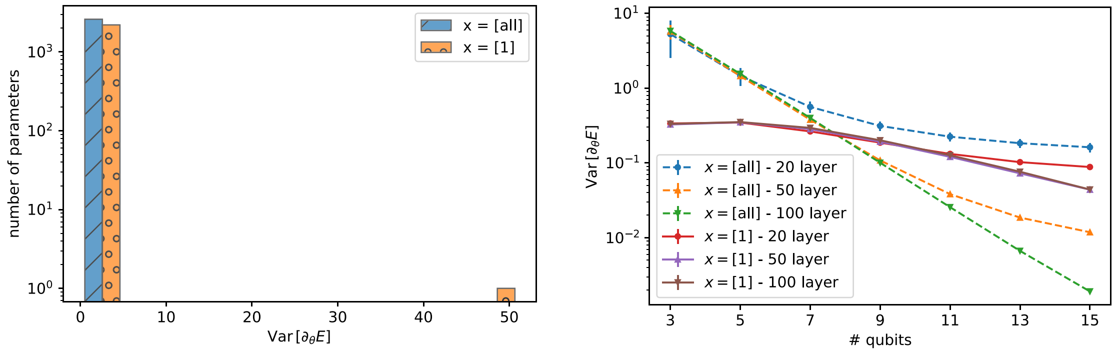

(a) (b)

Figure 15. (a) Number of parameters with similar variance of gradient for $x = [1]$ (reduced ansatz) and $x = [\text{all}]$ (full ansatz) for 9 qubits and 100 layers in the case with impurity. The large variance value corresponds to the first rotation parameter at the impurity qubit. (b) Average variance of gradient over all parameter choices excluding the parameter of the first impurity rotation angle. The error bars are the variance across the different gradient components.

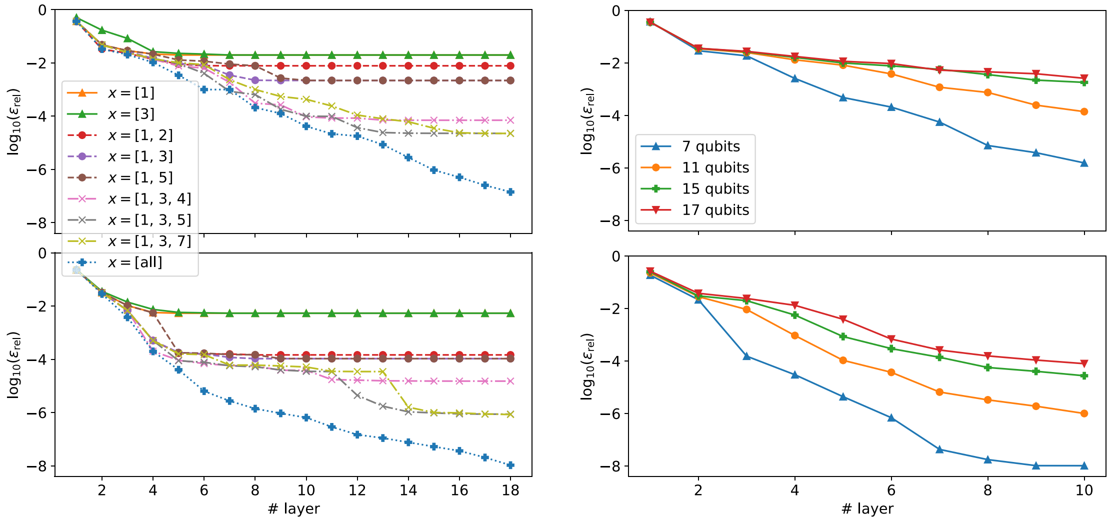

(a) (b)

Figure 16. (a) Accuracy obtained by the VQE for the XXZ model at the critical point without impurity, $h_0^z = 0$, (top) and with impurity, $h_0^z = -10$, (bottom) for 9 qubits compared to the exact result in a logarithmic plot. Results for different x are shown. (b) Accuracy depending on the number of layers for the XXZ model with $x = [\text{all}]$ for varying system size without impurity, $h_0^z = 0$, (top) and with impurity, $h_0^z = -10$, (bottom).

Appendix B. Second impurity model: XXZ chain

As comparison to the TFIM we also study the behavior of the XXZ model with an impurity to show that the results obtained are rather generic. Its Hamiltonian is given by

$$H_{\rm XXZ} = \sum_{i=-L/2}^{L/2} \left(\sigma_i^x \sigma_{i+1}^x + \sigma_i^y \sigma_{i+1}^y + \Delta \sigma_i^z \sigma_{i+1}^z\right) + h_0^z \sigma_0^z \tag{B1}$$

with an anisotropy Δ and the Pauli matrices $\sigma^{x,y,z}$. Similarly to the TFIM, we add a term for a longitudinal field at the central qubit. This model is gapped for $|\Delta| > 1$. For $\Delta < -1$, the qubits are aligned ferromagnetically, while for $\Delta > 1$, they are aligned antiferromagnetically along the z-direction. For $-1 \leqslant \Delta \leqslant 1$, the system is in a critical phase and is described by a conformal field theory with central charge $c = 1$. We choose $\Delta = 0.5$, which is far off from the Heisenberg point as well as from the gapped phase.

As before, we compare the results obtained with VQE with results found numerically by diagonalization and we use open boundary conditions to separate the chain with increasing impurity strength.

An overview of the results for 9 qubits in the XXZ model is shown in figure 16(a). Overall, we find a similar behavior for the XXZ model, although less clear as for the TFIM. A key difference is in the placement of the entangling gates between the subsystems: better results are achieved when the entanglement gates are applied in every odd layer, e.g. $x = [1, 3, 5]$.

To investigate the halving of layers needed to reach exponential improvement, we compute the accuracy depending on the number of layers for $x = [\text{all}]$ for various system sizes, visualized in figure 16(b).

Without impurity, we see again a finite-depth regime followed by a finite-size regime depending linearly on the system size. Note that the distinction was very clear for the TFIM while for the XXZ model it is not as clear. With impurity, we find also for the XXZ model that the finite-depth regime is halved similarly our result for the TFIM.

The data of the plateau values for $x = [1], x = [1, 3]$ and $x = [1, 3, 5]$ for increasing system sizes are plotted in figure 17. The results match with those of the TFIM: upon increasing the number of layers in x, the accuracy of the result increases for all chain lengths. Without impurity, the plateau values are higher than with impurity, although not as much as in the case of the TFIM. Note that in general, for the XXZ model it is more difficult to achieve high precision in the minimization process and more iterations are necessary. This significantly increases the simulation time. Therefore, only system sizes up to 13 qubits are simulated.

To better understand why the difference of the plateau values for the XXZ model is not as pronounced in the presence of an impurity as it was for the TFIM, we plot the exact entanglement entropy, obtained by numerical diagonalization, as function of h_0^z and the relative energy error $\varepsilon_{\rm rel}$ for $x = [1]$ and $x = [1, 3]$ in figure 18(a). With increasing magnetic field strength, the entanglement entropy decreases and in parallel the

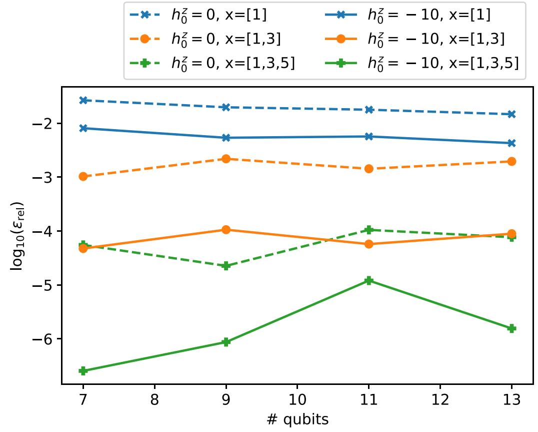

Figure 17. Logarithmic accuracy obtained with the VQE compared to the exact result for different system sizes and number of layers in x for the XXZ model at $\Delta = 0.5$. The number of x also indicates the number of cuts necessary to divide the circuit. Thus, one can read off the number of cuts necessary to achieve a given accuracy, e.g. to achieve an accuracy in the order of 10^{-4} for the model with impurity two cuts are needed.

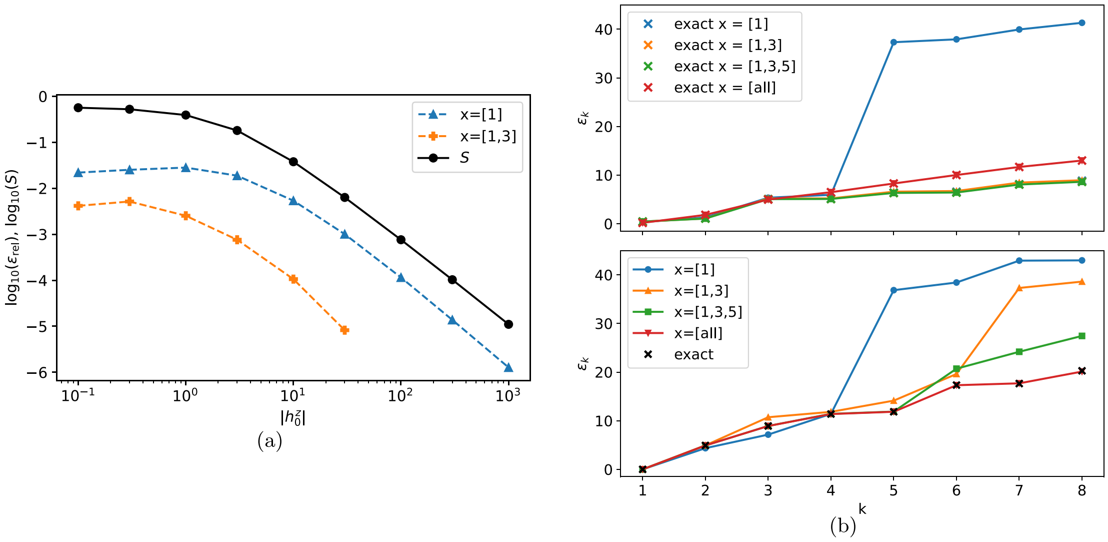

(a)

(b)

Figure 18. (a) Logarithmic accuracy obtained with the VQE at the plateau for $x = [1]$ compared to entanglement entropy for varying impurity strength for the XXZ model with 9 qubits. (b) Eigenvalues ε_k of the entanglement Hamiltonian for the XXZ model at $\Delta = 0.5$ with 7 qubits without $h_0^z = 0$, (top) and with impurity, $h_0^z = -10$, for 13 layers for different x compared to the exact solution. In the case with impurity, different exact solutions, which are given by the largest overlap of the vector found by VQE and the linear combination of the exact calculation are present due to a degeneracy. This degeneracy is broken for finite h_0^z.

accuracy improves, following the same trend as for the TFIM. However, much larger impurity values are needed to significantly reduce the entanglement entropy.

In figure 18(b), the entanglement spectrum is shown for the XXZ model with 7 qubits with and without impurity for 13 layers for different x. Without impurity, there is a degeneracy of the ground state energy, which implies that we have a linear combination of potential eigenvectors $|\psi'(\vec{\theta})\rangle$ that can be approximated by the VQE. Therefore, in this case we use the linear combination of the exact calculation with the largest overlap with the vector found by the VQE. With this linear combination of the exact solution we calculate the exact entanglement spectrum meaning that we can have multiple exact spectra depending on what the largest overlap is. These are then compared to the results obtained by VQE calculation. Using this method we find similar results as for the TFIM: the more layers are included in x, the more accurately the eigenvalues are found starting from the smallest ones. Again, with impurity the difference between the first two eigenvalues increases indicating separation of the qubit chain. However, the entanglement eigenvalues of the XXZ model with impurity remain small compared to those of the TFIM. This means that the XXZ chain is more entangled than the TFIM chain for the same value of h_0^z, which aligns with the results of the entanglement entropy.

ORCID iDs

Alina Joch https://orcid.org/0009-0001-9391-6653
Götz S Uhrig https://orcid.org/0000-0003-1961-0346
Benedikt Fauseweh https://orcid.org/0000-0002-4861-7101

References

[1] Feynman R P 1982 Simulating physics with computers *Int. J. Theor. Phys.* **21** 467
[2] Fauseweh B 2024 Quantum many-body simulations on digital quantum computers: state-of-the-art and future challenges *Nat. Commun.* **15** 2123
[3] Preskill J 2018 Quantum computing in the NISQ era and beyond *Quantum* **2** 79
[4] Salathé Y *et al* 2015 Digital quantum simulation of spin models with circuit quantum electrodynamics *Phys. Rev. X* **5** 021027
[5] Lanyon B P *et al* 2011 Universal digital quantum simulation with trapped ions *Science* **334** 57
[6] Barends R *et al* 2015 Digital quantum simulation of fermionic models with a superconducting circuit *Nat. Commun.* **6** 7654
[7] Fauseweh B and Zhu J-X 2021 Digital quantum simulation of non-equilibrium quantum many-body systems *Quantum Inf. Process.* **20** 138
[8] Bharti K *et al* 2022 Noisy intermediate-scale quantum algorithms *Rev. Mod. Phys.* **94** 015004
[9] Cerezo M *et al* 2021 Variational quantum algorithms *Nat. Rev. Phys.* **3** 625
[10] Kandala A, Mezzacapo A, Temme K, Takita M, Brink M, Chow J M and Gambetta J M 2017 Hardware-efficient variational quantum eigensolver for small molecules and quantum magnets *Nature* **549** 242
[11] Higgott O, Wang D and Brierley S 2019 Variational quantum computation of excited states *Quantum* **3** 156
[12] Barison S, Vicentini F and Carleo G 2021 An efficient quantum algorithm for the time evolution of parameterized circuits *Quantum* **5** 512
[13] Fauseweh B and Zhu J-X 2023 Quantum computing Floquet energy spectra *Quantum* **7** 1063
[14] Peruzzo A, McClean J, Shadbolt P, Yung M-H, Zhou X-Q, Love P J, Aspuru-Guzik A and O'Brien J L 2014 A variational eigenvalue solver on a photonic quantum processor *Nat. Commun.* **5** 4213
[15] Bravo-Prieto C, Lumbreras-Zarapico J, Tagliacozzo L and Latorre J I 2020 Scaling of variational quantum circuit depth for condensed matter systems *Quantum* **4** 272
[16] McClean J R, Boixo S, Smelyanskiy V N, Babbush R and Neven H 2018 Barren plateaus in quantum neural network training landscapes *Nat. Commun.* **9** 4812
[17] Lyu C, Montenegro V and Bayat A 2020 Accelerated variational algorithms for digital quantum simulation of many-body ground states *Quantum* **4** 324
[18] Tkachenko N V, Sud J, Zhang Y, Tretiak S, Anisimov P M, Arrasmith A T, Coles P J, Cincio L and Dub P A 2021 Correlation-informed permutation of qubits for reducing ansatz depth in the variational quantum eigensolver *PRX Quantum* **2** 020337
[19] Tilly J *et al* 2022 The variational quantum eigensolver: a review of methods and best practices *Phys. Rep.* **986** 1
[20] Robin C E P and Savage M J 2023 Quantum simulations in effective model spaces: Hamiltonian-learning variational quantum eigensolver using digital quantum computers and application to the Lipkin-Meshkov-Glick model *Phys. Rev. C* **108** 024313
[21] Hengstenberg S M, Robin C E P and Savage M J 2023 Multi-body entanglement and information rearrangement in nuclear many-body systems: a study of the Lipkin–Meshkov–Glick model *Eur. Phys. J. A* **59** 231
[22] Crippa A, Jansen K and Rinaldi E 2024 Analysis of the confinement string in $(2+1)$-dimensional quantum electrodynamics with a trapped-ion quantum computer (arXiv:2411.05628 [hep-lat])
[23] Lyu C, Tang X, Li J, Xu X, Yung M-H and Bayat A 2023 Variational quantum simulation of long-range interacting systems *New J. Phys.* **25** 053022
[24] Affleck I, Laflorencie N and Sørensen E S 2009 Entanglement entropy in quantum impurity systems and systems with boundaries *J. Phys. A: Math. Theor.* **42** 504009
[25] Prodan E, Hughes T L and Bernevig B A 2010 Entanglement spectrum of a disordered topological chern insulator *Phys. Rev. Lett.* **105** 115501
[26] Torlai G, Tagliacozzo L and Chiara G D 2014 Dynamics of the entanglement spectrum in spin chains *J. Stat. Mech.* 06001
[27] Wiersema R, Zhou C, de Sereville Y, Carrasquilla J F, Kim Y B and Yuen H 2020 Exploring entanglement and optimization within the Hamiltonian variational ansatz *PRX Quantum* **1** 020319
[28] Sun R-Y, Shirakawa T and Yunoki S 2023 Efficient variational quantum circuit structure for correlated topological phases *Phys. Rev. B* **108** 075127
[29] Du Y, Hsieh M-H, Liu T and Tao D 2020 Expressive power of parametrized quantum circuits *Phys. Rev. Res.* **2** 033125
[30] Sim S, Johnson P D and Aspuru-Guzik A 2019 Expressibility and entangling capability of parameterized quantum circuits for hybrid quantum-classical algorithms *Adv. Quantum Technol.* **2** 1900070
[31] Orús R 2019 Tensor networks for complex quantum systems *Nat. Rev. Phys.* **1** 538
[32] Clark S R 2018 Unifying neural-network quantum states and correlator product states via tensor networks *J. Phys. A: Math. Theor.* **51** 135301
[33] Luo X-Z, Liu J-G, Zhang P and Wang L 2020 Yao.jl: extensible, efficient framework for quantum algorithm design *Quantum* **4** 341
[34] Mogensen P K and Riseth A N 2018 Optim: a mathematical optimization package for Julia *J. Open Source Softw.* **3** 615
[35] Haegeman J 2024 KrylovKit
[36] Pfeuty P 1970 The one-dimensional ising model with a transverse field *Ann. Phys., NY* **57** 79
[37] Dutta A, Aeppli G, Chakrabarti B K, Divakaran U, Rosenbaum T F and Sen D 2015 Quantum phase transitions in transverse field spin models: from statistical physics to quantum information (arXiv:1012.0653 [cond-mat.stat-mech])
[38] Bravyi S, Smith G and Smolin J A 2016 Trading classical and quantum computational resources *Phys. Rev. X* **6** 021043
[39] Peng T, Harrow A W, Ozols M and Wu X 2020 Simulating large quantum circuits on a small quantum computer *Phys. Rev. Lett.* **125** 150504
[40] Mitarai K and Fujii K 2021 Constructing a virtual two-qubit gate by sampling single-qubit operations *New J. Phys.* **23** 023021
[41] Holmes Z, Sharma K, Cerezo M and Coles P J 2022 Connecting ansatz expressibility to gradient magnitudes and barren plateaus *PRX Quantum* **3** 010313

[42] Ramírez G, Rodríguez-Laguna J and Sierra G 2015 Entanglement over the rainbow *J. Stat. Mech.* 06002

[43] Alba V, Santalla S N, Ruggiero P, Rodriguez-Laguna J, Calabrese P and Sierra G 2019 Unusual area-law violation in random inhomogeneous systems *J. Stat. Mech.* 023105

[44] Vatan F and Williams C 2004 Optimal quantum circuits for general two-qubit gates *Phys. Rev. A* **69** 032315

[45] Ma S-K, Dasgupta C and Hu C-K 1979 Random antiferromagnetic chain *Phys. Rev. Lett.* **43** 1434

[46] Dasgupta C and Ma S-K 1980 Low-temperature properties of the random Heisenberg antiferromagnetic chain *Phys. Rev. B* **22** 1305

[47] Refael G and Moore J E 2004 Entanglement entropy of random quantum critical points in one dimension *Phys. Rev. Lett.* **93** 260602

[48] Crognaletti G, Di Bartolomeo G, Vischi M and Loris Viteritti L 2024 Equivariant variational quantum eigensolver to detect phase transitions through energy level crossings *Quantum Sci. Technol.* **10** 015048

[49] Laflorencie N 2005 Scaling of entanglement entropy in the random singlet phase *Phys. Rev. B* **72** 140408

[50] Gray J 2018 quimb: a python package for quantum information and many-body calculations *J. Open Source Softw.* **3** 819

[51] Anderson P W 1961 Localized magnetic states in metals *Phys. Rev.* **124** 41

[52] Kondo J 1964 Resistance minimum in dilute magnetic alloys *Prog. Theor. Phys.* **32** 37

[53] Piquard C, Glidic P, Han C, Aassime A, Cavanna A, Gennser U, Meir Y, Sela E, Anthore A and Pierre F 2023 Observing the universal screening of a Kondo impurity *Nat. Commun.* **14** 7263

[54] Defenu N, Donner T, Macrì T, Pagano G, Ruffo S and Trombettoni A 2023 Long-range interacting quantum systems *Rev. Mod. Phys.* **95** 035002

[55] Buchheit A A, Keßler T, Schuhmacher P K and Fauseweh B 2023 Exact continuum representation of long-range interacting systems and emerging exotic phases in unconventional superconductors *Phys. Rev. Res.* **5** 043065